Estimation of Wind Direction in Tropical Cyclones using C-band Dual-Polarization Synthetic Aperture Radar

Shengren Fan[1], Biao Zhang[1], Alexis Mouche[2], William Perrie[3], Jun A. Zhang[4]

[1]School of Marine Sciences, Nanjing University of Information Science and Technology, Nanjing, China

[2]Laboratoire d'Oc´eanographie Physique Spatiale, Ifremer, Plouzane, France

[3]Bedford Institute of Oceanography, Fisheries and Oceans Canada, Dartmouth, Nova Scotia, Canada

[4]Hurricane Research Division at NOAA/AMOL and CIMAS at University of Miami, Florida, USA

for publication in

IEEE Transactions on Geoscience and Remote Sensing

*Corresponding Author:

Prof. Dr. Biao Zhang

School of Marine Sciences

Nanjing University of Information Science and Technology

219 Ningliu Road, Nanjing, 210044, CHINA

Email: zhangbiao@nuist.edu.cn

Abstract

Under extreme weather conditions, the imprints of kilometer-scale marine atmospheric boundary layer roll vortices on the ocean surface are clearly visible in synthetic aperture radar (SAR) images of storms. Therefore, storm wind direction information can be obtained by analyzing SAR image features caused by boundary layer rolls. VH-polarized SAR imagery captures the structural features of storms well and shows prominent image gradients along the radial directions of the storm. The signal-to-noise ratios of VH-polarized images are small in low wind speed areas, but they are large in same regions of VV-polarized images. Thus, there is the potential to retrieve the storm's wind directions using a combination of the VH- and VV-polarized SAR observations. In this study, we use the local gradient method to estimate tropical cyclone wind directions from C-band RADARSAT-2 and Sentinel-1A dual-polarization (VV+VH) SAR imagery. As a case study, wind directions with spatial resolution of 12.5 km are derived by using both wide-swath VV- and VH-polarized SAR imagery over two hurricanes (Earl and Bertha) and one Typhoon (Meranti). We compare wind directions derived from 10 dual-polarization SAR images with collocated wind directions from buoys, scatterometer, radiometer, and Hurricane Research Division Real-time Hurricane Wind Analysis System (H*Wind) data. Statistical comparisons show that the wind direction bias and root-mean-square error are 5.62° and 27.13° for VV-polarization, 4.36° and 23.40° for VH-polarization, 3.47° and 22.76° for VV and VH-polarization, suggesting dual-polarization SAR is more suitable for the estimation of tropical cyclone wind directions than VV or VH-polarization SAR.

Index Terms—Tropical Cyclone, Wind Direction, Synthetic Aperture Radar (SAR)

I. Introduction

In order to better understand tropical cyclone (TC) intensity and to track wind field structure evolution, there is a need for a continuous monitoring of tropical cyclones. Due to its high spatial resolution, wide swath acquisitions, and its capability to operate at day and night, C-band Spaceborne Synthetic Aperture Radar (SAR) microwave sensors have been proven to be very promising. Moreover, C-band SARs operate at low frequency (~5.3 GHz). Therefore SAR signals are not severely impacted by rain and cloud, even when observing TCs [1]. Over the last decade, a great deal of effort has been devoted to the derivation of TC wind fields. This has been fostered by the recent opportunity to have acquisitions in both co- and cross-polarization thanks to RADARSAT-2 and Sentinel-1 SAR missions [2-7].

For low and moderate winds, co-polarization (VV or HH) SAR wind speed retrievals are based on geophysical model functions (GMFs) derived from scatterometers. Since there are two unknown parameters (wind speed and direction) and only one single non-rotational antenna, the inverse problem is under-constrained. To overcome this limitation of SAR systems, the wind direction is generally set before retrieving the wind speed. In general, the Navy Operational Global Atmospheric Prediction System (NOGAPS) model can be used to provide wind direction inputs for SAR wind speed retrievals [8]. This method tends to produce physically reasonable estimates when the time difference (between model output and SAR acquistion time) is lower than 1.5 hours. However, the weather forecast model spatial resolution is generally far less (0.125°) than what is achieved for SAR (about 500 m to 1 km). Scatterometer wind direction is also a candidate external source for SAR wind speed retrieval [9]. But scatterometer observations are contaminated by land backscattering in coastal areas and cannot provide accurate wind directions in these areas. Moreover, scatterometer data are not always available for collocation with every SAR acquisition. Furthermore, both methods have the risk of possible inaccuracies in wind direction due to interpolation; when interpolating data from the model or scatterometer wind direction to a given SAR pixel, there maybe spatial or temporal differences between the SAR data and the external source. In the case of translating and rotating phenomena such as TCs, the interpolation may become unreliable.

When we rely only on SAR images, it is sometimes possible to extract wind directions from kilometer-scale wind streaks due to marine atmospheric boundary layer (MABL) rolls [10-11] or wind-driven Langmuir circulations [12]. The direction of the wind streaks can be determined by using the Fast Fourier transform (FFT) method [10, 13-15], the local gradient (LG) method [16-17], or the wavelet transform (WT) method [18]. The wind directions derived from these approaches have a 180° ambiguity, which can be resolved by examining the wind shadowing visible on the lee of the coastlines, or by other sources such as atmospheric models or *in situ* measurements [14-15]. A previous study reported that the FFT method determines the wind direction with a root-mean-square-error (RMSE) of ±24° when compared to *in situ* wind measurements [13]. The wind directions derived from the LG method were also compared with those from a numerical weather forecast model, leading to a RMSE of 21.6° [17]. However, both FFT and LG wind direction retrieval methods are limited when there is a lack of wind streaks imaged by the SAR, especially at low wind speeds; one study indicated that MABL rolls were present in 44% of 1,882 SAR images and completely absent in 34% [19]. Furthermore, in another recent study, ~48.0% of a data set of 227 SAR images displayed wind streaks; among those images, 67.3%, 20.0%, and 12.7% occurred under unstable, neutral, and stable atmospheric conditions, respectively [20].

For strong winds, MABL rolls are prevalent in the TC boundary layer. The surface imprints of kilometer-scale roll vortices is clearly visible in the SAR images of hurricanes [21-22]. In particular, 3 to 6 km wavelength roll vortices have been associated with secondary circulations between the main TC rain bands [1]. Other studies show that SAR can provide useful information for identifying TC MABL rolls and found that streak patterns in ocean surface roughness can be explained by changes in surface wind speed that are caused by the formation of rolls [11, 21, 23]. The direction of these streaks is assumed to be parallel to the wind direction [16, 24]. Thus, it is possible to retrieve wind directions from TC SAR images containing wind rolls. Researchers have used the LG method or the FFT method to obtain hurricane wind directions from the streaks in SAR images acquired only at VV-polarization [2, 25], but the retrieved wind directions were not validated using *in situ* measurements, scatterometer or radiometer observations, or atmospheric model simulations. Moreover, VV-polarized radar backscatter is saturated as wind speeds approach hurricane-force winds. Therefore, the signatures of wind streaks may not be very clear between the TC eye and eyewall where the strongest winds generally occur. Compared to VV-polarization, radar backscatter acquired at VH-polarization is much less sensitive to radar incidence angle or wind direction and increases as wind speed increases, especially in TCs [4] and particularly near TC eyes (see Figures 2 (b) and (c) in [7]). Furthermore, VH-polarized radar backscattering does not show obvious saturation even when the wind speed is close to 50 m/s [5-7]. High backscatter in the eyewall area and low backscatter in the eye and peripheral regions are clearly found in the VH-polarized SAR TC images (see Figure 3 in [26]). The advantage of VV-polarization over VH-polarization is that the former has higher Signal to Noise Ratio (SNR) in low wind speed areas than the latter. This low SNR is expected to affect the detection of streaks in cross-polarization images for the lowest wind speeds. Therefore, a combination of both VV- and VH-polarization SAR measurements is probably necessary to fully exploit the potential of both polarizations and to maximize TC wind direction retrievals in SAR images. Note that a different and complementary approach [27] has also been recently proposed to combine SAR backscattering with Doppler measurements in order to minimize the use of external data for wind field retrieval. This method is not considered here and requires an accurate attitude control system of the satellite platform and the antenna pointing direction in order to properly get the geophysical contribution to the Doppler centroid estimated from SAR.

The goal of this paper is to retrieve hurricane wind direction without ambiguity based on the computation of local gradients over the wind-induced streaks in SAR imagery. Our approach is to use C-band RADARSAT-2 and Sentinel-1A VV- and VH-polarized SAR images. The benefit of using each polarization is discussed and the retrieved wind directions are validated against buoy observations, scatterometer or radiometer measurements, and also compared with H*Wind data. The remainder of this paper is organized as follows. Section II describes the data set. In Section III, the method for wind direction retrieval is introduced. In Section IV, we present the wind direction retrieval and validation results. Finally, the summary and conclusions are given in Section V.

II. Data Set

For this study we collected 10 RADARSAT-2 and Sentinel-1A SAR images of TCs in the North Atlantic Ocean, East Pacific Ocean, and West Pacific Ocean. These images were collocated with wind measurements from *in situ* buoys, scatterometer or radiometer measurements, or TC wind analysis products. Table I summarizes the SAR images and the collocated wind data. We use this collocated data set to validate SAR-derived wind directions.

A. RADARSAT-2 and Sentinel-1A SAR data

C-band RADARSAT-2 SAR can provide single-polarization (HH, VV, HV, or VH), dual-polarization (VV+VH or HH+HV), and quad-polarization (HH+HV+VH+VV) imaging modes with different swath coverage. This study focuses on measurements from the dual-polarization (VV+VH) ScanSAR wide-imaging mode, which provides wide swath (500 km) images suitable for monitoring TCs from space. ScanSAR wide mode has a range of incidence angles between 20° and 49°. The pixel spacing is 50 m × 50 m and the resolution is 163–73 m and 78–106 m (range by azimuth). The Noise Equivalent Sigma Zero (NESZ) of this mode is about 28±2 dB [28]. Moreover, we also collected Sentinel-1A dual-polarization SAR imagery, which was acquired in extended wide swath (EW) imaging mode. The EW swath is 400 km wide and covers incidence angles from about 23.7° through 44.5°. The pixel spacing is 40 m × 40 m and the resolutions are 90.8–95.1 m and 90.1–90.13 m in the range and azimuth directions, respectively. The NESZ of this mode ranges from -26 to -37 dB and decreases with increasing incidence angle [29]. We note that the two sensors have comparable NESZ.

B. QuikSCAT data

We use QuikSCAT surface wind fields from the Remote Sensing Systems (RSS) website (www.remss.com/mission/qscat/). QuikSCAT Level 3 (L3) data consists of global grid values of meridional and zonal components of winds, measured twice a day at approximately 0.25° × 0.25° resolution, which is suitable for scientific applications. The mission requirements for QuikSCAT have an accuracy of 2 m/s RMSE for wind speeds in the range 3–20 m/s, 10% RMSE for the range 20–30 m/s, and 20° RMSE in wind direction for wind speeds ranging from 3–30 m/s [30-31]. QuikSCAT ocean wind vectors have been completely reprocessed using the new Ku-band GMF termed as Ku-2011. This has greatly improved both wind speed and direction for strong winds, showing a significant benefit for QuikSCAT Ku-2011 wind directions at high wind speeds up to 35 m/s (RMSE=9°), compare to the Ku-2001 (RMSE=15°) [32].

C. WindSat data

WindSat has been designed to show the capability of polarimetric microwave radiometry to measure ocean wind vectors [33]. By using multiple polarimetric channels (10–37 GHz, plus a linearly polarized channel at 6.8 GHz), WindSat has been very successful in measuring both wind speed and wind direction. An all-weather algorithm capable of global wind vector retrievals even in storm conditions was developed for WindSat [34]. The wind direction retrieval accuracy varies from about 10° in light rain to 30° in heavy rain. The radiometer wind direction accuracy decreases significantly in heavy rain because of the strong attenuation of the signal. WindSat all-weather wind vector products with spatial resolution of 0.25° × 0.25° can be acquired through the RSS website (http://www.remss.com/missions/windsat/).

*D. H*Wind data*

HRD H*Wind data are gridded tropical cyclone wind analysis products based on a wide range of observations [35-36]. The H*Wind product provides an estimate of the wind field based on all available observations from a vast array of marine, land, aircraft, and satellite platforms. H*Wind assimilates all of the available wind observations from a specific time period into a moving “storm relative” coordinate system that allows for the production of an objectively blended wind field. The spatial and temporal resolutions of the H*Wind product are about 6 km and 3 hours, respectively. For hurricanes, a series of statistical analyses show that the total uncertainty in the H*Wind product is ~6% near the storm center and increases to nearly 13% near the radius for tropical storm force winds [37].

E. Buoy data

Four SAR images were collocated with National Data Buoy Center buoys located in the North Atlantic and the East Pacific Oceans. These buoys measured wind speeds and directions and reported values averaged over 8-min periods each hour. In each case, the buoys are located within the image footprint, and the SAR acquisition time is within 30 minutes of the buoy measurement. Moreover, in order to observe the upper ocean response to typhoons we used a cross-shaped array of five moored buoys and four subsurface moorings that had been deployed in the Northern South China Sea in September 2014. Typhoon Rammasun passed over one of the buoys and was simultaneously imaged by RADARSAT-2.

III. Methodology

The ideal image of a wind streak is about constant along its direction and strongest varying about orthogonal to its direction. Since the gradient is always the direction of strongest increase, the direction of a wind streak is approximately orthogonal to the gradient direction. Therefore, the wind direction, which is assumed to be parallel to the wind streak, is set to be perpendicular to the direction of the gradient. In this study, we use the LG method [16] to estimate wind directions from C-band dual-polarization TC SAR images. This method computes the LGs and chooses the orthogonal of the most frequently computed gradient direction as a possible wind direction. We remove 180° wind direction ambiguity based on TC wind field structure characteristics.

A. SAR image smoothing and re-sampling

Since multiplicative speckle noise is present in SAR images, any gradient direction could be present if this noise is dominating. However, there is preference toward the correct orthogonal direction. To improve our chances of choosing the correct orthogonal direction we need to first eliminate the noise in the SAR images. This is carried out by twice smoothing and re-sampling of an image with operators B^2 and B^4 before calculating LGs. The first image smoothing is performed with the following convolution operation:

$$A' = B^4 A \tag{1}$$

where A is the SAR amplitude image, B^4 is a binomial operator for the smoothing operation in various directions, namely:

$$B^4 = \frac{1}{256}\begin{bmatrix} 1 & 4 & 6 & 4 & 1 \\ 4 & 16 & 24 & 16 & 4 \\ 6 & 24 & 36 & 24 & 6 \\ 4 & 16 & 24 & 16 & 4 \\ 1 & 4 & 6 & 4 & 1 \end{bmatrix} . \qquad (2)$$

Similar to the FFT method [13] for wind direction extraction, where the search is for the signal of the wind streaks, for wavelengths from 500 to 1500 m, the gradients are generally calculated on SAR images reduced to 100-, 200-, and 400-m pixel spacings. In some cases, ocean surface wave patterns are clearly visible in SAR images, which are somehow similar to wind streaks, but on different spatial scales. The wave-induced linear features are possibly affecting the image gradient estimation process, and thus wind direction retrieval. Previous investigation suggested that images of the open ocean should be smoothed and re-sampled to 200-m pixel spacing when long ocean waves are present in SAR images [16]. This processing can eliminate ocean surface wave interference when calculating the local maximum gradients induced by wind streaks. All SAR images used in our study were acquired in the open ocean over TCs with expected wavelengths for ocean waves between 200 and 350 m. Therefore we reduced all SAR images to 200-m pixel spacing images. The image re-sampling is done with isotropic low-pass filters. The re-sampled image is referred to as A''. The second image smoothing is implemented by using the following convolution operation:

$$A'' = B^2 A' \qquad (3)$$

where

$$B^2 = \frac{1}{16}\begin{bmatrix} 1 & 2 & 1 \\ 2 & 4 & 2 \\ 1 & 2 & 1 \end{bmatrix} \quad . \tag{4}$$

B. Computing the Local Gradients

Depending on the properties of the marine boundary layer, the spacing of the MABL rolls in the cross-wind direction varies from 1 to 9 km [16]. Thus, we first divide the SAR amplitude image into a number of sub-images, each of which covers an area of 25 × 25 km^2, before performing the LG computations. Subsequently, the gradient components of each sub-image are computed with the Scharr operator [38]

$$D_x = \frac{1}{32}\begin{bmatrix} 3 & 0 & -3 \\ 10 & 0 & -10 \\ 3 & 0 & -3 \end{bmatrix} \tag{5}$$

and its transpose

$$D_y = D_x^T. \tag{6}$$

Using Equations (5) and (6), the gradients are computed from the smoothed and re-sampled amplitude image A'',

$$G' = (g'_{mn}) = \left(D_x + iD_y\right)(A'') \tag{7}$$

where m and n denote the subscripts of the gradient image. The squared gradient is referred to as G'',

$$G'' = \left(g''_{m'n'}\right) = SR(g'^2_{mn}) \quad . \tag{8}$$

In Equation (8) SR represents the smoothing and re-sampling operations, which are done following the same procedure as the SAR amplitude image processing described in Section III. A. The values m' and n' denote the subscripts of the re-sampled squared gradient image. Gradients and squared gradients are stored as complex numbers, and therefore, any gradient and its negative yield the same value. This operation is compensated latter by taking the square root, but in the meanwhile, this process provides the capability to address any special considerations for 180° ambiguities. The magnitude of the squared gradients is expressed as G''', namely

$$G''' = \left(g'''_{m'n'}\right) = SR(|g'^2_{mn}|). \tag{9}$$

From the triangle inequality, it is clear that the magnitude of the average G'' is smaller than the average of the magnitude G''', and the better the squared gradients agree, the smaller the difference. Wherever the gradient is nonzero, we form the quotient in Equation (10), in order to measure directional coherency,

$$0 \le c_{m'n'} = \frac{\left|g''_{m'n'}\right|}{g'''_{m'n'}} \ll 1 \tag{10}$$

The directional coherency is considered to be the first quality criteria of the gradient estimation and is computed based on Equations (8) and (9).

C. Extracting the Main Directions

The main direction of a sub-image is determined by the maximum location in the smoothed histogram of the weighted local gradients. To establish the reliable points belonging to a selected sub-image, the second quality criteria is computed from the magnitude of the squared gradients,

$$0 \ll r_{m'n'} = \frac{\left|g''_{m'n'}\right|}{\left|g''_{m'n'}\right| + median\left(\left|g''_{p'q'}\right|\right)} < 1 \qquad . \tag{11}$$

In Equation (11), p' and q' denote the subscripts of the selected sub-image. The second term in the denominator is the median of the magnitudes of the squared gradients for the selected sub-image.

The directional values are sorted into 72 directional intervals of 5° each. For each interval, the Weighted and Squared Local Gradients (WSLG) are estimated as follows:

$$WSLG_{m'n'} = \frac{G''_{m'n'}}{|G''_{m'n'}|}(c_{m'n'} + r_{m'n'}) \quad . \tag{12}$$

This histogram is smoothed with the terms $B_{8x}^2 B_{4x}^2 B_{2x}^2 B_x^2$ from Equation (4) and interpolated. The definitions of these operators are given by Equations (13) – (16) below:

$$B_x^2 = \frac{1}{4}(1 \;\; 2 \;\; 1) \tag{13}$$

$$B_{2x}^2 = \frac{1}{4}(1 \;\; 0 \;\; 2 \;\; 0 \;\; 1) \tag{14}$$

$$B_{4x}^2 = \frac{1}{4}(1 \;\; 0 \;\; 0 \;\; 0 \;\; 2 \;\; 0 \;\; 0 \;\; 0 \;\; 1) \tag{15}$$

$$B_{8x}^2 = \frac{1}{4}(1 \;\; 0 \;\; 0 \;\; 0 \;\; 0 \;\; 0 \;\; 0 \;\; 0 \;\; 2 \;\; 0 \;\; 0 \;\; 0 \;\; 0 \;\; 0 \;\; 0 \;\; 0 \;\; 1) \quad . \tag{16}$$

The maximum of the magnitudes on the interpolated histogram gives the main squared gradient; the square root gives the main gradient; and the orthogonal to the main gradient defines the main direction to be searched, which still retains the 180° ambiguity.

Fig.1 shows a RADARSAT-2 dual-polarization SAR image acquired over Typhoon Meranti on September 12, 2016, at 21:28 UTC. As shown in Fig. 1, the VH-polarization SAR image is better able to delineate the typhoon structure features due to modifications of the ocean surface waves, than VV-polarization. This is because cross-polarized radar backscatters are much less sensitive to ocean surface wind directions and incidence angles than VV. In Fig.1, the incidence angle dependency of

VV explains the strong and non-geophysical contrast observed in the SAR image in the range direction. Based on Equation (12), we estimated the WSLG within a 25-km sub-image indicated by a red box in the VV- and VH-polarized SAR images.

Figs. 2(a) and 2(b) illustrate histograms of estimated WSLG magnitudes for VV- and VH-polarizations for this particular sub-image. The histogram of the WSLG for the 72 directional bins is found to exhibit more directional variation for the VH data than for the VV data. This illustrates the higher sensitivity of VH polarization to the signature of wind rolls than VV polarization. The dominant squared gradient is defined as the maximum of the smoothed histogram. To qualify the WSLG of each sub-image, we introduce a minimum threshold for the maximum of the smoothed WSLG magnitude. Based on an analysis of all available SAR imagery for the maximum WSLG, this threshold is set at a constant value of 45. Below this value, the LG estimation is considered as poor quality.

Taking account of all available SAR images we also analyze the variation of WSLG magnitudes with radar incidence angles. This is presented in Figs. 3(a) and 3(b), respectively for VV and VH polarizations. We observe that the maximum WSLG increases with incidence angles for VV. In particular, for comparatively larger incidence angles (40~49°), the maximum WSLG for VV are much larger than 45. This is can be explained by the higher relative impact of Bragg waves (centimeter waves which are more sensitive than longer waves) to the co-polarization NRCS variations at C-band, as the incidence angle increases [39]. On the contrary, the maximum WSLG is found to be close to, or below, 45 for VH. The weak dependence of the WSLG on incidence angle is certainly due to the weak incidence angle dependence of the NRCS. Moreover, the low SNR explains why the maximum WSLG amplitude is generally lower in VH than in VV. Therefore, we propose to combine maximum WSLG estimates from VV- and VH-polarizations to retrieve the wind direction from the highest quality WSLG. The estimated maximum WSLG of each sub-image for the entire collection of SAR images presented in Fig. 1 is shown in Fig. 4. The blank areas indicate that the maximum of the smoothed WSLG magnitude in the sub-image is below the threshold mentioned above. As observed, there is a complementarity between the two polarizations (see Figs. 4(a) and 4(b)). In particular we observe higher quality for WSLG near the hurricane eye in VH than in VV. We also note more blank areas far from the hurricane center in VH than in VV. Thus, after combination of both VV- and VH-polarization SAR measurements, the areas left with poor quality of WSLG are reduced (see Fig. 4(c)).

The direction corresponding to the square root of the maximum of the smoothed WSLG gives the orientation of the main gradient in each sub-image. Since wind direction is perpendicular to the main gradient direction, the wind direction (with 180° ambiguity) in each sub-image is then directly derived from the main gradient direction.

D. Wind direction ambiguity removal

The wind direction ambiguities are removed by assuming the expected TC wind direction structure in the northern hemisphere (this study is only dealing with TCs in this hemisphere) as shown in Fig. 5. The wind direction ambiguity removal procedure is divided into three steps: (1) Determine the TC eye center position based on the technique proposed in [40]. (2) Ascertain the quadrant for the appropriate sub-image under consideration, according to the positions of the eye center and the position of this specific sub-image. (3) Derive the unique wind direction based on the following criteria:

If (subimage is in first quadrant), then $270^{\mathrm{o}} < \Phi < 360^{\mathrm{o}}$

If (subimage is in second quadrant), then $0^{\mathrm{o}} < \Phi < 90^{\mathrm{o}}$

If (subimage is in third quadrant), then $90^{\mathrm{o}} < \Phi < 180^{\mathrm{o}}$

If (subimage is in forth quadrant), then $180^{\mathrm{o}} < \Phi < 270^{\mathrm{o}}$.

where Φ is the wind direction.

E. Interpolation

Figs. 6(a) and 6(b) shows the SAR-derived wind directions for Typhoon Meranti based on only VV- or VH-polarized SAR images, respectively. For VH wind direction retrieval, most of the areas where no wind direction can be derived correspond to large incidence angles associated with low wind speeds. The combination of VV- and VH-polarized SAR images yields the results shown in Fig. 6(c). As expected, the wind directions in Fig. 6(c) are now much better resolved, compared to Figs. 6(a) or 6(b). However, areas without wind directions are still evident, associated with WSLG magnitudes lower than 45. To overcome this issue, we apply a bi-linear interpolation to obtain wind directions for the entire image.

IV. Results and Discussion

In this study, we first applied the LG method to retrieve wind directions in TCs. Subsequently, we now assess our methodology for SAR-retrieved wind directions using collocated wind directions from buoys, QuikSCAT, WindSat, and H*Wind data.

In the case of Typhoon Meranti, we collocated the RADARSAT-2 SAR observation with WindSat measurements, to illustrate the methodology, as discussed in the previous section. The time interval between SAR observation and WindSat measurements is 22 minutes. The determination of collocation is based on the nearest distance criteria. To validate wind direction results, we choose only the points where the distances between SAR retrievals and WindSat measurements are smaller than 0.1°. Fig. 7 illustrates the wind directions from our dual-polarization SAR retrievals and those from WindSat measurements. Quantitative comparisons between SAR-retrieved wind directions and WindSat measurements, are shown in Fig. 8. Wind directions from VV-polarized SAR have a bias of −3.72° and an RMSE of 24.15°; for VH-polarized SAR, the bias and RMSE are 1.31° and 23.01°; whereas for dual-polarized SAR, the bias and RMSE are -1.07° and 20.43°, respectively.

Fig. 9 shows a RADARSAT-2 dual-polarization SAR image acquired over Hurricane Bertha on July 12, 2008, at 10:14 UTC. The SAR-retrieved wind directions are shown in Fig. 10. This example also shows the complementarity of the two polarizations, both far from, and close to, the hurricane eye area. Fig. 11 illustrates the wind directions from dual-polarization SAR retrievals and the collocated QuikSCAT measurements. For this case, the time interval between the SAR image and the QuikSCAT observations is 32 minutes. Fig. 12 shows a comparison between SAR-retrieved and QuikSCAT-measured wind directions. Wind directions from VV-polarized SAR have a bias of 4.39° and an RMSE of 22.29°; for VH-polarized SAR, the bias and RMSE are 3.98° and 26.27°; whereas for dual-polarized SAR, the bias and RMSE are 3.84° and 16.21° after interpolation, respectively. Since SAR and QuikSCAT operate at different frequencies (C- and Ku-band), apparent differences between SAR retrievals and QuikSCAT measurements of wind direction can be found at individual points. Moreover, this difference is also possibly caused by the wind direction interpolation operator. We also note that under very high wind conditions, heavy rainfall is prominent in the hurricane eyewall region which can induce inaccurate QuikSCAT wind directions in this area, which may explain some of the differences between SAR and scatterometer measurements.

Fig. 13 shows a RADARSAT-2 dual-polarization SAR image acquired over Hurricane Earl on September 2, 2010, at 22:59 UTC. Since no available radiometer and scatterometer wind measurements could be matched up to the SAR images of Hurricane Earl, we used collocated SAR retrievals and H*Wind data to evaluate the accuracy of the wind direction retrieval. For Hurricane Earl, H*Wind data were acquired on September 2, 2010, at 22:30 UTC. Fig. 14 shows SAR-retrieved wind directions. Fig.15 illustrates the wind directions from dual-polarization SAR retrievals and those from collocated H*Wind data. For this case, the time interval between the SAR image and the H*Wind data is 29 minutes. Fig. 16 shows a comparison between SAR-retrieved and H*Wind estimates for wind directions. Wind directions from VV-polarized SAR have a bias of -14.42° and an RMSE of 38.83°; for VH-polarized SAR, the bias and RMSE are -20.94° and 28.55°; whereas for dual-polarized SAR, the bias and RMSE are 20.93° and 27.78°. One should keep in mind that part of this difference was due to location mismatch between the SAR and the H*Wind data. This can introduce large differences in typhoons with high temporal and spatial variations. Of course it is worth mentioning that the H*Wind wind directions do not exactly represent ground truth, because they are derived from the flight-level observations of wind direction by subtracting a constant angle.

In addition to case-by-case validation for 10 SAR images, we also perform a statistical comparison between SAR-retrieved wind directions and those measured from buoy, radiometer, scatterometer, and H*Wind data. The total number of collocated data pairs is 2,045. As shown in Fig. 17, wind directions from VV-polarized SAR have a bias of 5.62° and an RMSE of 27.13°; for VH-polarized SAR, the bias and RMSE are 4.36° and 23.40°; whereas for dual-polarized SAR, the bias and RMSE are 3.47° and 22.76°. Both the case study and the statistical results show that dual-polarization is always better than VV or VH for the retrieval of TC wind directions. In the future, we plan to conduct more TC wind direction validation studies, when additional reliable measurements become available. There are several important factors that affect the VV- and VH-polarized SAR wind direction retrieval accuracy. The NESZ impact on the normalized radar cross section (NRCS) is one of these. There is also potential inter-channel cross talk for dual-polarization data which cannot be corrected [41]. Investigations have demonstrated that the strongest wind regions within TCs are usually accompanied by significant rain [42]. Heavy rain contamination and additional effects associated with severe sea states can strongly dampen the VV- and VH-polarized NRCS [43-45], and thus affect the image gradient estimation for wind direction retrieval. However, the application of other parameters directly extracted from the SAR image, such as the geophysical Doppler contribution, may also lead to improvements in the wind field retrieval. In particular, geophysical signature in the Doppler contribution acquired in cross-polarization imagery over hurricanes remains to be documented and its potential needs to be investigated.

V. Summary and Conclusion

The retrieval of the ocean surface wind fields from single-antenna SAR missions is an under constrained inverse problem. The use of possibly inaccurate wind directions can lead to large errors in SAR wind speed retrievals. Estimating the wind direction directly from the SAR image is thus an attractive approach. Indeed kilometer-scale wind streaks are frequently visible in SAR images due to MABL rolls or wind-driven Langmuir circulations, especially in TC conditions. For high winds, clear image contrasts (gradients) can be found in cross-polarized TC SAR images. Such gradients provide a good opportunity to derive wind directions using SAR images acquired in cross-polarization mode.

We applied the LG method to retrieve TC wind directions by using both VV- and VH-polarized SAR imagery. The spatial resolution of SAR-derived wind direction is 12.5 km. Our analysis reveals that, as implemented, the LG method is dependent on the incidence angle in VV-polarization data and more accurate for low to medium wind speed regimes. By comparison, VH-polarization does not seem sensitive to incidence angles but is more reliable for the strongest wind speeds. The SAR-retrieved wind directions have been quantitatively compared data from collocated buoys, radiometer, scatterometer, and H*Wind estimates. Statistical comparison results show that wind direction bias and RMSE are 5.62° and 27.13°, respectively, for VV-polarization, and 4.36° and 23.40°, respectively, for VH-polarization, and 3.47° and 22.76°, respectively, for dual-polarization. This suggests that SAR images acquired in dual-polarization are better than those in either VV- or VH-polarization to derive wind directions in storms. There are several causes for differences between wind direction estimates from SAR retrieval and collocated wind measurement data, including: (1) NESZ impact on NRCS, (2) potential cross talk between VV and VH channels, and (3) NRCS attenuation due to heavy rainfall.

In this study, no manual intervention was required for wind direction retrieval. Moreover, we automatically removed the 180° ambiguity using characteristics of the expected TC wind direction structure. However, the validation of SAR-derived wind direction in storms is still a challenging problem because too few SAR TC images can be collocated with data from buoy, radiometer, scatterometer, or H*Wind measurements. It is thus necessary to collect more SAR imagery and auxiliary data to assess the LG method for wind direction retrieval under storm conditions.

Acknowledgments: The authors would also like to thank the European Space Agency for providing Sentinel-1A data and the Canadian Space Agency for providing RADARSAT-2 data. This work was supported by the National Key R&D Program of China [Grant 2016YFC1401001], the National Science Foundation of China for Outstanding Young Scientist [Grant 41622604], the Excellent Youth Science Foundation of Jiangsu Province [Grant BK2016090], the International Cooperation, CAS, Chinese-Foregin Cooperation in Key Project [Grant 133337KYSB20160002], and the Data Utilization Application Plan [DUAP] of the Canadian Space Agency. The NOAA buoy data is downloaded from http://www.ndbc.noaa.gov/.

References

[1] Katsaros, K. B., P. W. Vachon, W. T. Liu and P. G. Black, Microwave remote sensing of tropical cyclones from space, *J. Oceanogr.*, vol. 58, pp. 137-151, 2002.

[2] Horstmann, J., D. R. Thompson, F. Monaldo, S. Iris, and H. C. Graber, Can synthetic aperture radars be used to estimate hurricane force wind?, *Geophys. Res. Lett.*, vol. 32, L22801, doi:10.1029/2005GL023992, 2005.

[3] Shen, H., W. Perrie, and Y. He, A new hurricane wind retrieval algorithm for SAR images, *Geophys. Res. Lett.*, vol. 33, L21812, doi:10.1029/2006GL027087, 2006.

[4] Zhang, B., and W. Perrie, Cross-polarized synthetic aperture radar: a new potential technique for hurricanes, *Bull. Amer. Meteor. Soc.*, vol. 93, pp. 531-541, doi:10.1175/BAMS-D-11-00001.1, 2012.

[5] Zhang, B., W. Perrie, Jun A. Zhang, E. Uhlhorn, and Y. He, High-resolution hurricane vector winds from C-band dual-polarization SAR observations, *J. Atmos. Oceanic Technol.*, vol. 31, pp. 272-286, doi:10.1175/JTECH-D-13-00006.1, 2014.

[6] Zhang, G., X. Li, W. Perrie, P. A. Hwang, B. Zhang and X. Yang, A hurricane wind speed retrieval model for C-band RADARSAT-2 cross-polarization ScanSAR images, *IEEE Trans. Geosci. Remote Sens.*, vol. 55, pp. 4766-4744, 2017.

[7] Mouche, A., B. Chapron, B. Zhang, B., and R. Husson, Combined co- and cross-polarized SAR measurements under extreme wind conditions, *IEEE Trans. Geosci. Remote Sens.*, vol. 55, pp. 6476-6755, 2017.

[8] Monaldo, F. M., D. R. Thompson, R. C. Beal, W. G. Pichel, and P. Clemente-Colón, Comparison of SAR-derived wind speed with model predictions and ocean

buoy measurements, *IEEE Trans. Geosci. Remote Sens.*, vol. 39, pp. 2587-2600, 2001.

[9] Shimada, T., H. Kawamura, M. Shimada, An L-band geophysical model function for SAR wind retrieval using JERS-1 SAR, *IEEE Trans. Geosci. Remote Sens.*, vol. 41, pp. 518-531, 2003.

[10] Gerling, T. W., Structure of the surface wind field from the Seasat SAR, *J. Geophys. Res.*, vol. 91, pp. 2308-2320, 1986.

[11] Alpers, W., and B. Brümmer, Atmospheric boundary layer rolls observed by the synthetic aperture radar aboard the ERS-1 satellite, *J. Geophys. Res.*, vol. 99, pp. 12613-12621, 1994.

[12] Leibovich, S., The form and dynamics of Langmuir circulation, *J. Fluid Mech.*, vol. 15, pp. 391-427, 1983.

[13] Vachon, P. W., and F. W. Dobson, Validation of wind vector retrieval from ERS-1 SAR images over the ocean, *Global Atmos. Ocean Syst.*, vol. 5, pp. 177-187, 1996.

[14] Lehner, S., J. Horstmann, W. Koch, and W. Rosenthal, Mesoscale wind measurements using recalibrated ERS SAR images, *J. Geophys. Res.*, vol. 103, pp. 7847-7856, 1998.

[15] Fetterer, F., D. Gineris, and C. C. Wackerman, Validating a scatterometer wind algorithm for ERS-1 SAR, *IEEE Trans. Geosci. Remote Sens.*, vol. 36, pp. 479-492, 1998.

[16] Koch, W., Directional analysis of SAR images aiming at wind direction, *IEEE Trans. Geosci. Remote Sens.*, vol. 42, pp. 702-710, 1994.

[17] Horstmann, J., W. Koch, S. Lehner, and R. Tonboe, Ocean winds from RADARSAT-1 ScanSAR, *Can. J. Remote Sensing*, vol. 28, pp. 524-533, 2002.

[18] Du, Y., W. Pachon, and J. Wolfe, Wind direction estimation from SAR images of the ocean using wavelet analysis, *Can. J. Remote Sensing*, vol. 28, pp. 498-509, 2002.

[19] Levy. G and R. A. Brown, Detecting planetary boundary layer rolls from SAR, in *Remote Sensing of the Pacific Ocean From Satellite*, R. A. Brown, Ed., pp. 128-134, 1998.

[20] Zhao, Y., X. Li, and J. Sha, Sea surface wind streaks in spaceborne synthetic aperture radar imagery, *J. Geophys. Res.*, vol. 121, pp. 6731-6741, 2016.

[21] Foster, R. C., Why rolls are prevalent in the hurricane boundary layer, *J. Atmos. Sci.*, vol. 62, pp. 2647-2661, 2005.

[22] Huang, L., X. Li, B. Liu, J. A. Zhang, D. Shen, Z. Zhang, W. Yu, Tropical cyclone boundary layer rolls in synthetic aperture radar, *J. Geophys. Res.*, vol. 123, doi:10.1029/2018JC013755.

[23] Zhang, J. A., K. B. Katsaros, P. G. Black, S. Lehner, J. R. French, and W. M. Drennan, Effects of roll vortices on turbulent fluxes in the hurricane boundary layer, *Bound.-Layer Meteor.*, vol. 128, pp. 173-189, 2008.

[24] Li, X., J. A. Zhang, X. Yang, W. G. Pichel, M. DeMaria, D. Long, and Z. Li, Tropical cyclone morphology from spaceborne synthetic aperture radar, *Bull. Amer. Meteor. Soc.*, vol. 94, pp. 215-230, 2013.

[25] Reppucci, A., S. Lehner, J. Schulz-Stellenfleth, and S. Brusch, Tropical cyclone intensity estimated from wide-swath SAR images, *IEEE Trans. Geosci. Remote Sens.*, vol. 48, pp. 1639-1649, 2010.

[26] Zhao, Y., A. Mouche, B. Chapron, N. Reul, Direct comparison between active C-band radar and passive L-band radiometer measurements: Extreme event cases, *IEEE Geosci. Remote Sens Lett.*, vol. 15, pp. 897-901, 2018.

[27] Mouche, A., F. Collard, B. Chapron, K. Dagestad, G. Guitton, J. A. Johannessen, V. Kerbaol, M. W. Hansen, On the use of doppler shift for sea surface wind retrieval from SAR, *IEEE Trans. Geosci. Remote Sens.*, vol. 50, pp. 2901-2909, 2012.

[28] Slade, B., RADARSAT-2 product description. MacDonald, Detwiler and Associates Ltd. Doc. RN-SP-52-1238, 46 pp. [Available at http://gs.mdacorporation.com/products/sensor/radarsat2/RS2_Product_Description.pdf], 2009.

[29] Mouche, A., B. Chapron, Global C-band Envisat, Radarsat-2 and Sentinel-1 SAR measurements in copolarization and cross-polarization, *J. Geophys. Res.*, vol. 120, pp. 7195-2707, 2015.

[30] Dunbar, R., and K. L. Perry, SeaWinds on QuikSCAT level 3 daily, gridded ocean wind vectors. JPL SeaWinds Project, Guide Doc. [Available online at ftp://podaac-ftp.jpl.nasa.gov/allData/quikscat/L3/jpl/docs/qscat_L3.pdf], 2001.

[31] Callahan, P. S., QuikSCAT science data product user’s manual: Overview and geophysical data products, version 3.0. JPL D-18053-RevA, 2006.

[32] Ricciardulli, L., and F. Wentz, A scatterometer geophysical model function for climate-quality winds: QuikSCAT Ku-2011, *J. Atmos. Oceanic Technol.*, vol. 32, pp. 1829-1846, 2015.

[33] Gaiser, P. W., and coauthors, The WindSat spaceborne polarimetric microwave radiometer: Sensor description and early orbit performance, *IEEE Trans. Geosci. Remote Sen.*, vol. 42, pp. 2347-2361, 2004.

[34] Meissner, T., and F. J. Wentz, Wind-vector retrievals under rain with passive satellite microwave radiometers, *IEEE Trans. Geosci. Remote Sen.*, vol. 47, pp. 3065-3083, 2009.

[35] Powell, M. D., S. H. Houston, L. R. Amat, N. Morisseau-Leroy, The HRD real time hurricane wind analysis system, *J. Wind Eng. Ind. Aerodyn.*, vol. 77&78, pp. 53-64, 1998.

[36] Powell, M. D., and Coauthors, Reconstruction of hurricane Katrina's wind fields fro storm surge and wave hindcasting, *Ocean Eng.*, vol. 37, pp. 26-36, 2010.

[37] Dinapoli, S. M., and M. A. Bourassa, Uncertainty and Intercalibration analysis of H*Wind, *J. Atmos. Oceanic Technol.*, vol. 29, pp. 822-833, 2012.

[38] Scharr, H., *Optimal operators in digital image processing*. PhD thesis, University of Heidelberg, Germany, 2000.

[39] Mouche, A., B. Chapron, N. Reul, A simplified asymptotic theory for ocean surface electromagnetic wave scattering, *Waves in Random and Complex Media*, vol. 17, pp. 321-341, 2007.

[40] Zhang, G., B. Zhang, W. Perrie, Q. Xu, and Y. He, A hurricane tangential wind profile estimation method for C-band cross-polarization SAR, *IEEE Trans. Geosci. Remote Sen.*, vol. 52, pp. 7186-7194, 2014.

[41] Touzi, R., P. W. Vachon, and J. Wolfe, Requirement on antenna cross-polarization isolation for the operational use of C-band SAR constellations in maritime surveillance, *IEEE Trans. Geosci. Remote Sen.*, vol. 7, pp. 861-865, 2010.

[42] Weissman, D. E., and M. A. Bourassa, The influence of rainfall on scatterometer backscatter within tropical cyclone environments-Implications on parameterization of sea-surface stress, *IEEE Trans. Geosci. Remote Sen.*, vol. 49, 4805-4814, 2011.

[43] Reppucci, A., S. Lehner, J. Schulz-Stellenfleth, and C. S. Yang, Extreme wind conditions observed by satellite aperture radar, *Int. J. Remote Sens.*, vol. 29, pp. 6129-6144, 2008.

[44] Zhang, G., X. Li, W. Perrie, B. Zhang, and L. Zhang, Rain effects on the hurricane observations over the ocean by C-band synthetic aperture radar, *J*. *Geophys*. *Res*., vol. 120, doi:10.1002/2015JC011044, 2015.

[45] Alpers, W., B. Zhang, A. Mouche, K. Zeng, P. W. Chan, Rain footprints on C-band synthetic aperture radar images of the ocean – Revisited, *Remote Sens*. *Environ*., vol. 187, pp. 169-185, 2016.

TABLE I

TC SAR IMAGES AND THE COLLOCATED WIND DATA FOR WIND DIRECTION RETRIEVAL AND VALIDATION

TC Name	Satellite	Date	Time (UTC)	Collocated wind data	Time (UTC)
Bertha	RS2	Jul 12 2008	10:14	QuikSCAT	09:42
Earl	RS2	Aug 30 2010	09:57	Buoy	10:00
Earl	RS2	Sep 2 2010	22:59	Buoy & H*Wind	23:00 & 22:30
Arthur	RS2	Jul 3 2014	11:13	Buoy	11:10
Rammasun	RS2	Jul 17 2014	10:27	Buoy	11:00
Edouard	RS2	Sep 14 2014	09:05	WindSat	09:30
Dophin	RS2	May15 2015	08:37	Buoy	08:42
Soudelor	RS2	Aug 3 2015	20:31	WindSat	21:06
Lester	S1A	Aug 31 2016	03:15	WindSat	03:00
Meranti	RS-2	Sep 12 2016	21:28	WindSat	22:00

RS2 and S1A denote RADARSAT-2 and Sentinel-1A, respectively.

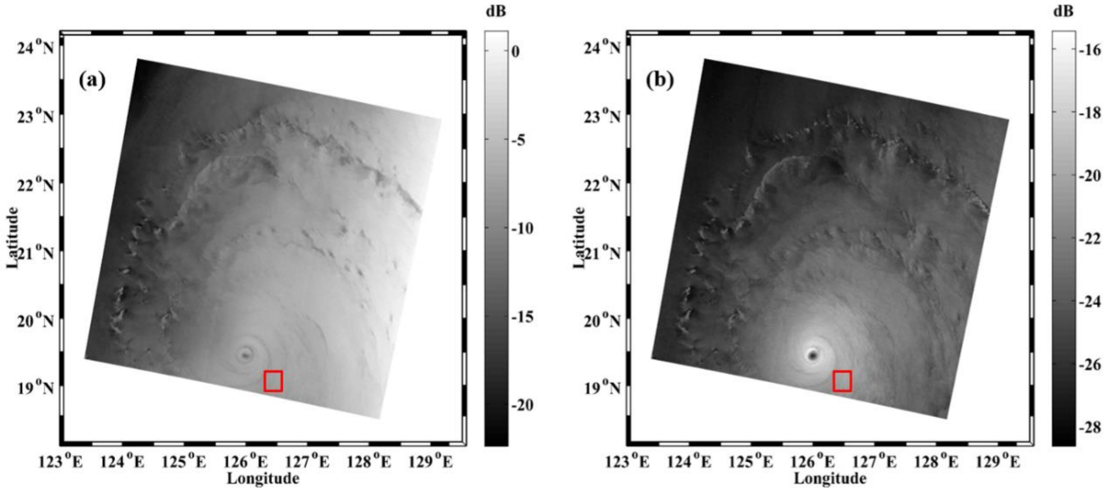

Fig. 1. RADARSAT-2 dual-polarization SAR image acquired over Typhoon Meranti on September 12, 2016, at 21:28 UTC showing (a) VV-polarization and (b) VH-polarization, where the color bar shows σ_0 (dB) in VV-polarization (σ_{VV}^0) and in VH-polarization (σ_{VH}^0), respectively. Red square denotes the selected sub-image (25 km×25 km). RADARSAT-2 Data and Product MacDonald, Dettwiler, and Associates Ltd., All Rights Reserved.

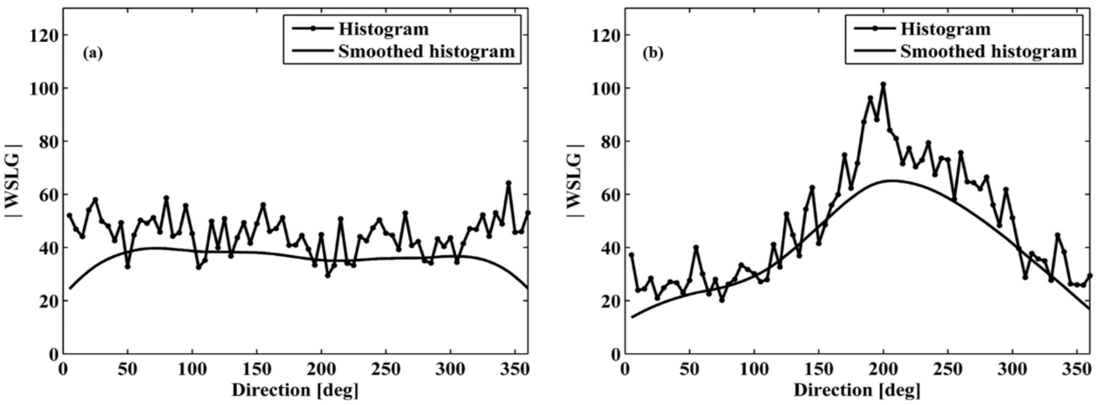

Fig. 2. Histogram of magnitudes of weighted and squared local gradients (WSLG) estimated with SAR sub-image acquired in (a) VV-polarization and (b) VH-polarization.

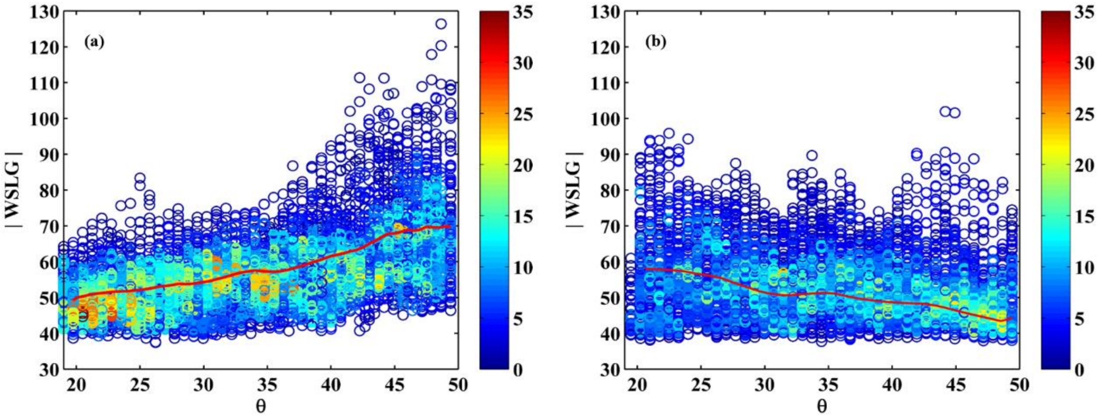

Fig. 3. The magnitudes of weighted and squared local gradients (WSLG) versus radar incidence angle, (a) VV-polarization and (b) VH-polarization.

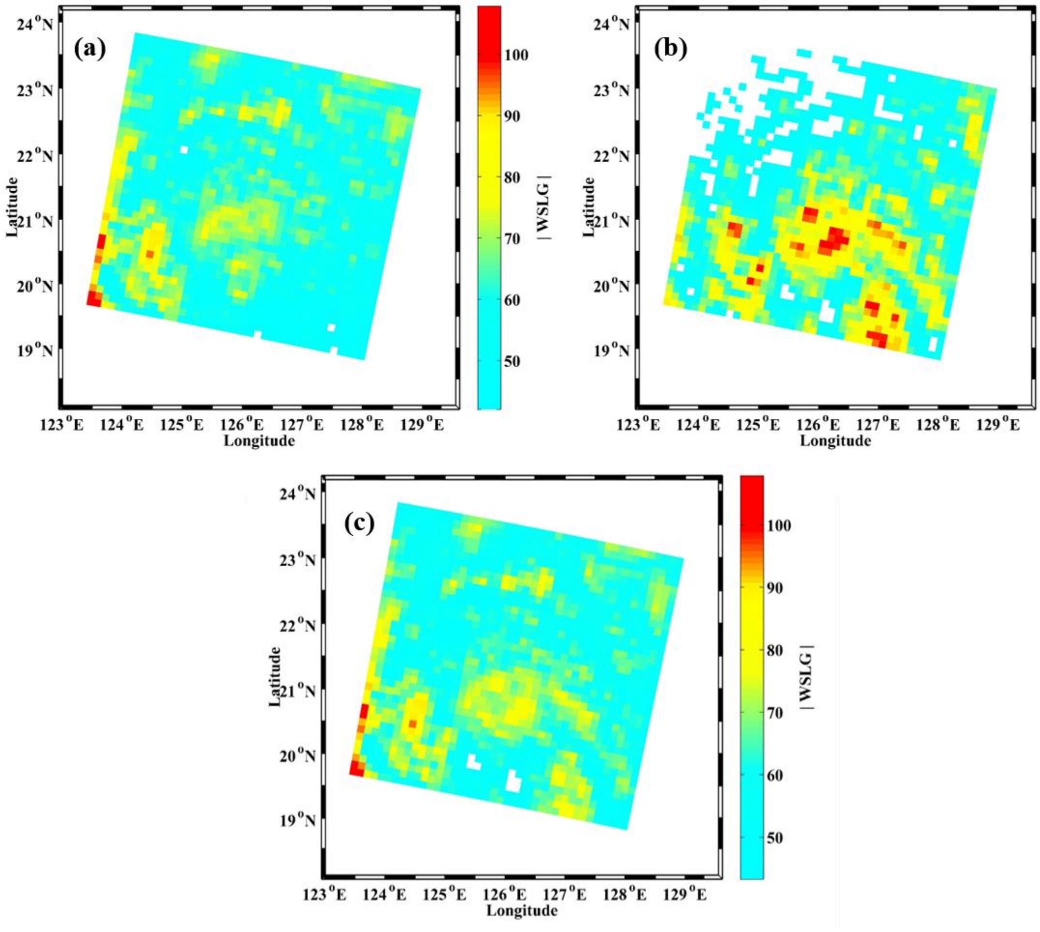

Fig. 4. Maximum of smoothed WSLG magnitude of Typhoon Meranti estimated with SAR image acquired in (a) VV-polarization, (b) VH-polarization, (c) Dual-polarization (VV+VH).

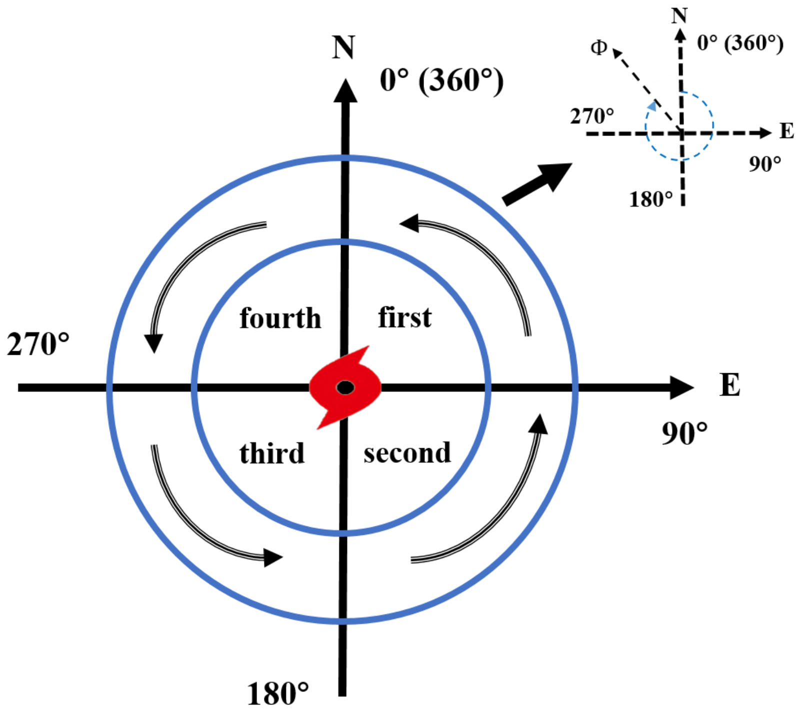

Fig. 5. Diagram of typical tropical cyclone wind direction structure in the northern hemisphere. The black arrows are wind directions.

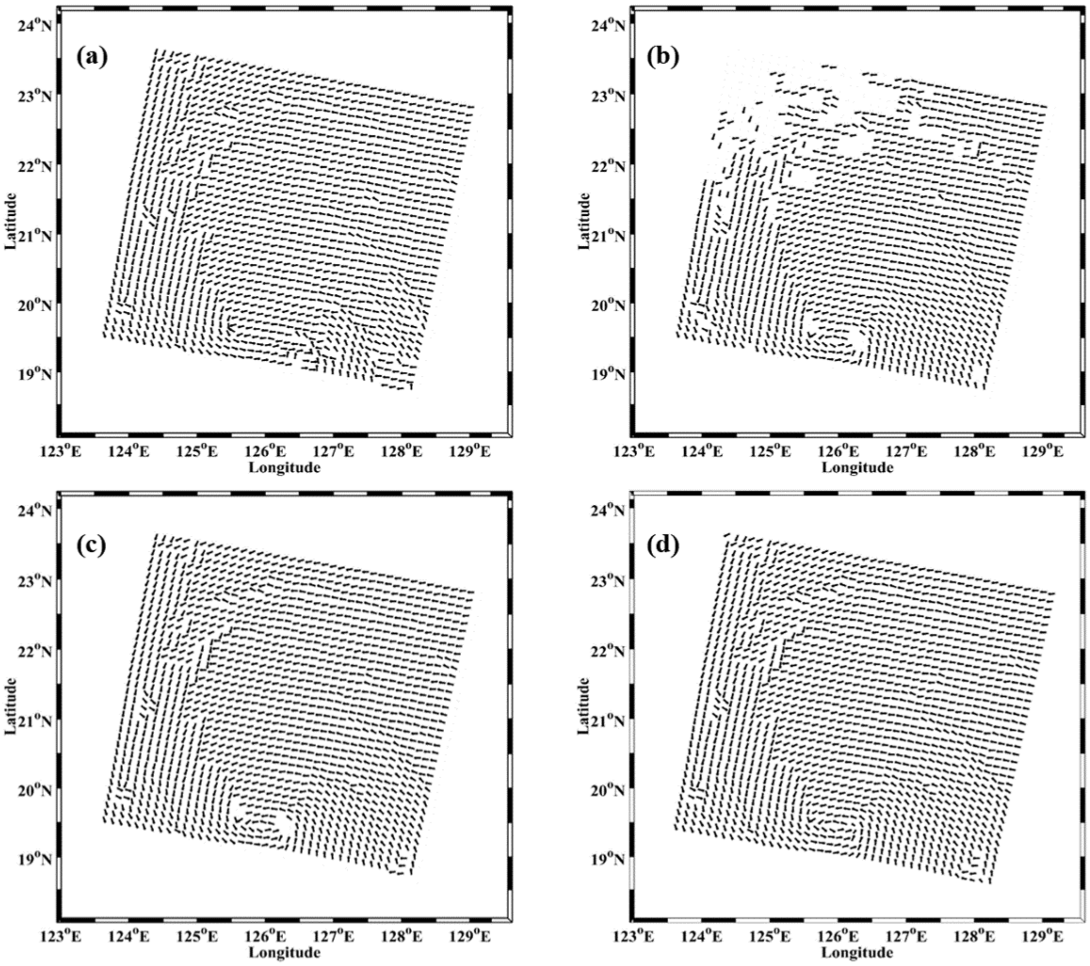

Fig. 6. SAR-retrieved wind directions of Typhoon Meranti on September 12, 2016, at 21:28 UTC, with image of (a) VV-polarization, and (b) VH-polarization, and (c) Dual-polarization (VV+VH), and (d) Dual-polarization (VV+VH) and interpolation processing.

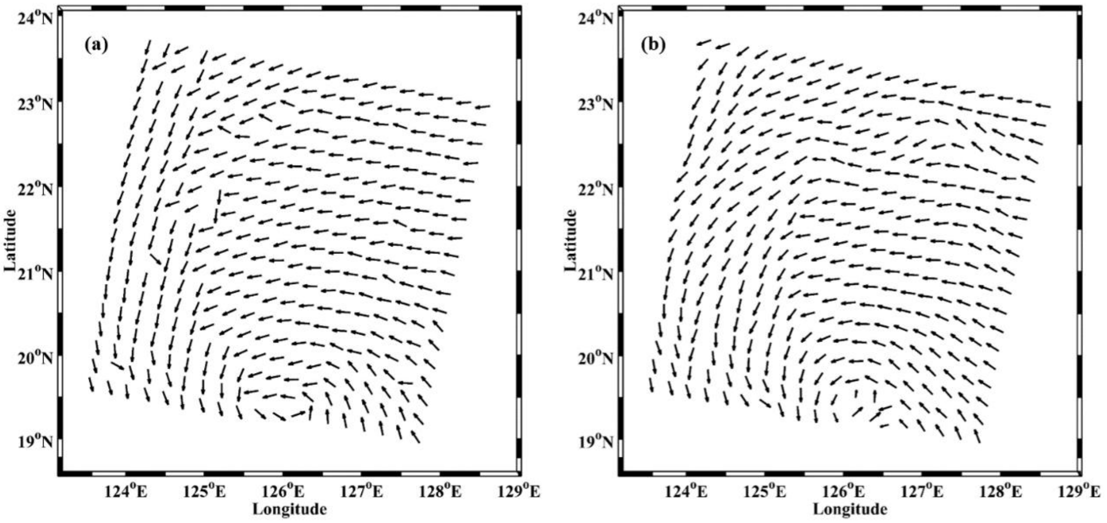

Fig. 7. (a) Dual-polarization SAR-retrieved wind directions of Typhoon Meranti on September 12, 2016, at 21:28 UTC. (b) WindSat-measured wind directions on September 12, 2016, at 22:00 UTC.

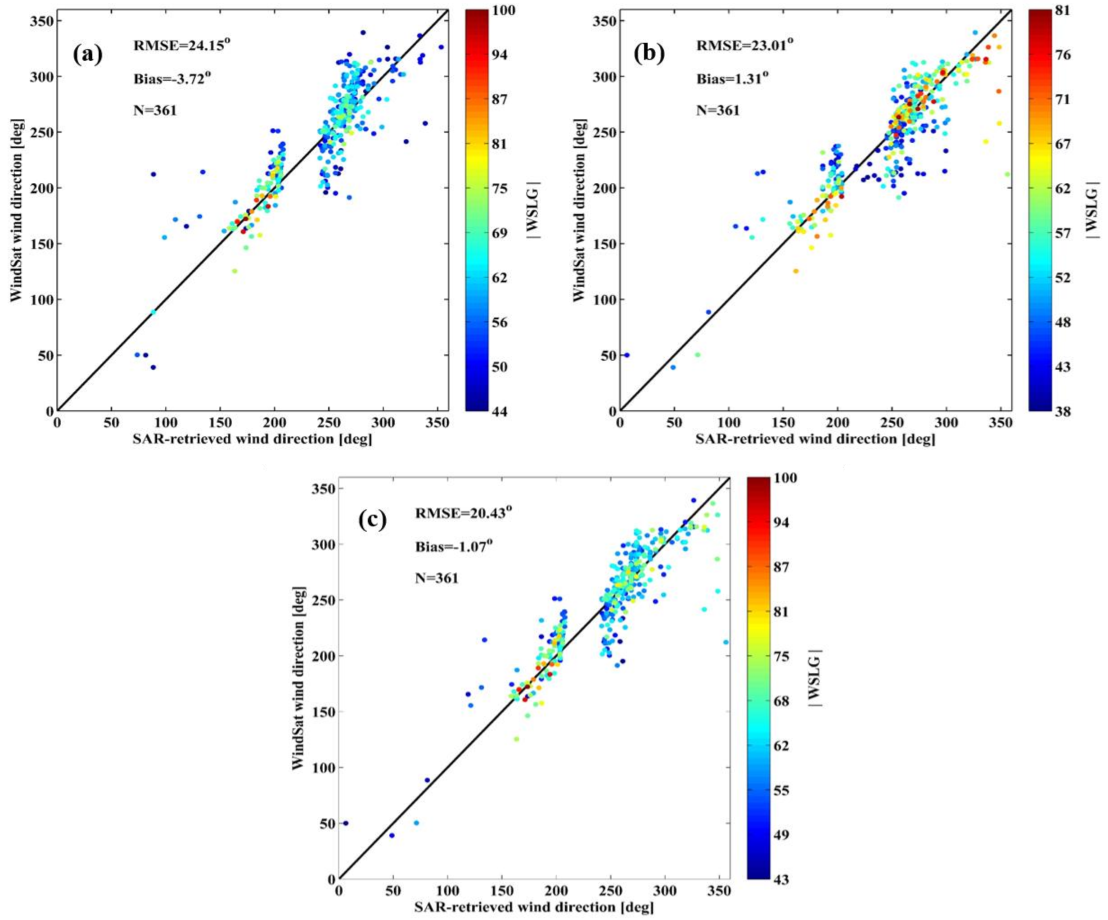

Fig. 8. VV-polarization SAR-retrieved wind directions versus WindSat-measured wind directions, and (b) VH-polarization SAR-retrieved wind directions versus WindSat-measured wind directions, and (c) Dual-polarization (VV+VH) SAR-retrieved wind directions versus WindSat-measured wind directions. Typhoon Meranti wind directions from SAR and WindSat are acquired on September 12, 2016, at 21:28 UTC, and on September 12, 2016, at 22:00 UTC, respectively.

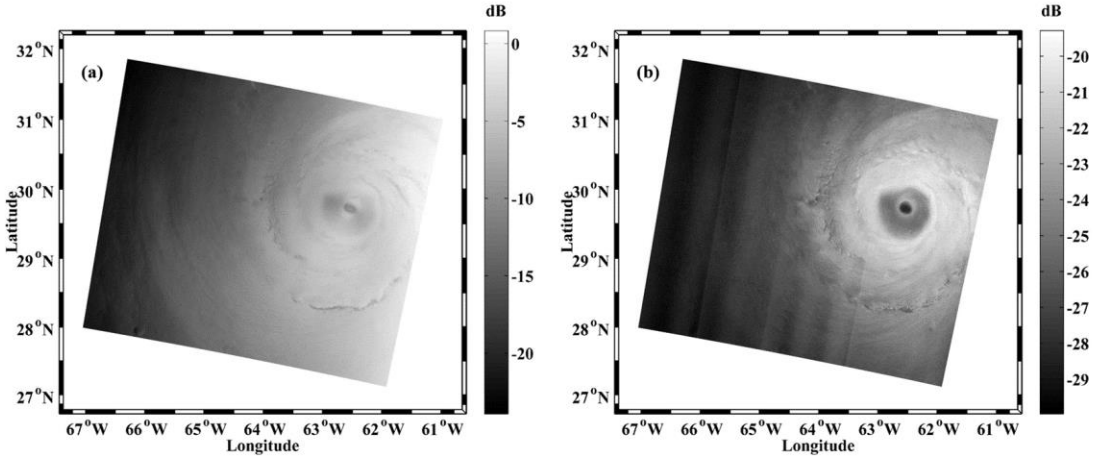

Fig. 9. RADARSAT-2 dual-polarization SAR image acquired over Hurricane Bertha on July 12, 2008, at 10:14 UTC showing (a) VV-polarization and (b) VH-polarization, where the color bar shows σ_0 (dB) in VV-polarization (σ_{VV}^0) and in VH-polarization (σ_{VH}^0), respectively. RADARSAT-2 Data and Product MacDonald, Dettwiler, and Associates Ltd., All Rights Reserved.

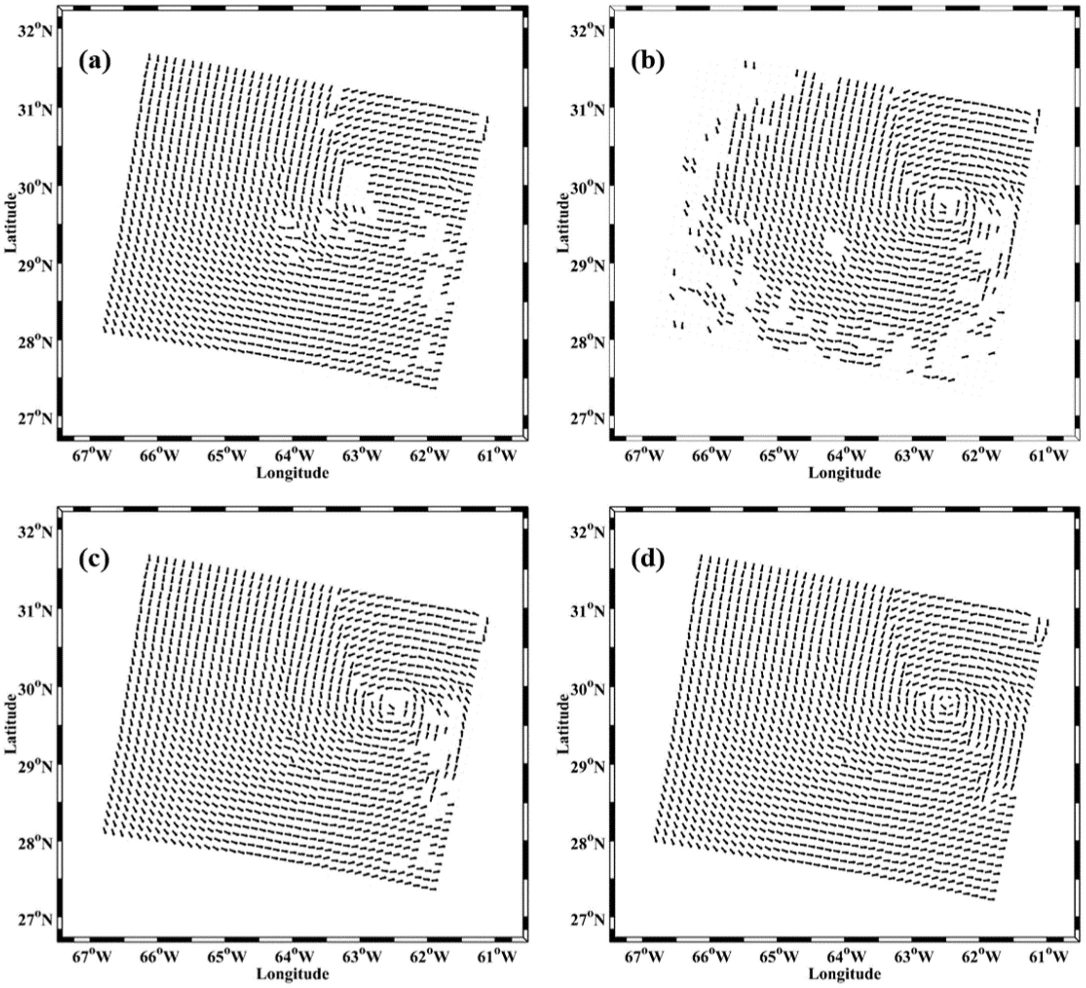

Fig. 10. SAR-retrieved wind directions of Hurricane Bertha on July 12, 2008, at 10:14 UTC, with image of (a) VV-polarization, and (b) VH-polarization, and (c) Dual-polarization (VV+VH), and (d) Dual-polarization (VV+VH) and interpolation processing.

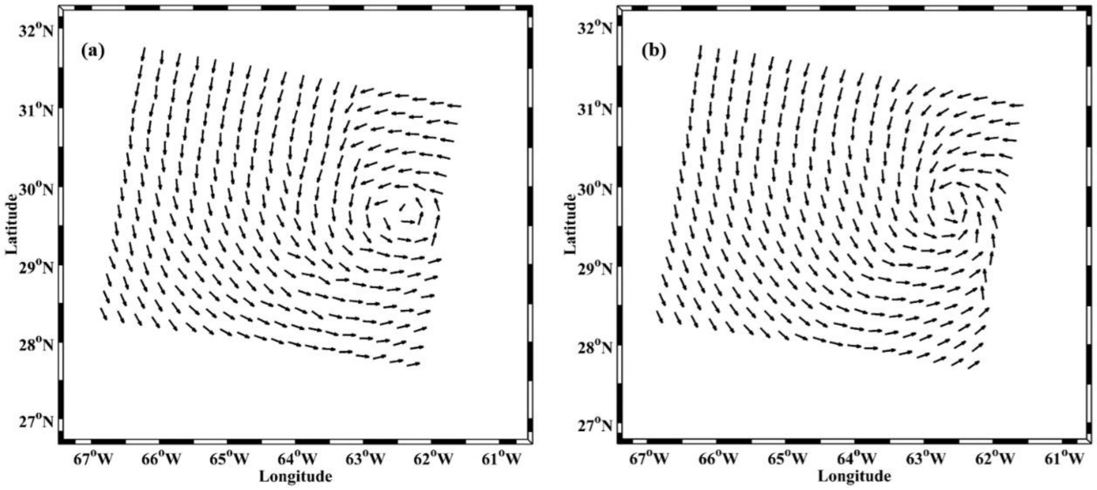

Fig. 11. (a) Dual-polarization SAR-retrieved wind directions of Hurricane Bertha on July 12, 2008, at 10:14 UTC. (b) QuikSCAT-measured wind directions on July 12, 2008, at 09:42 UTC.

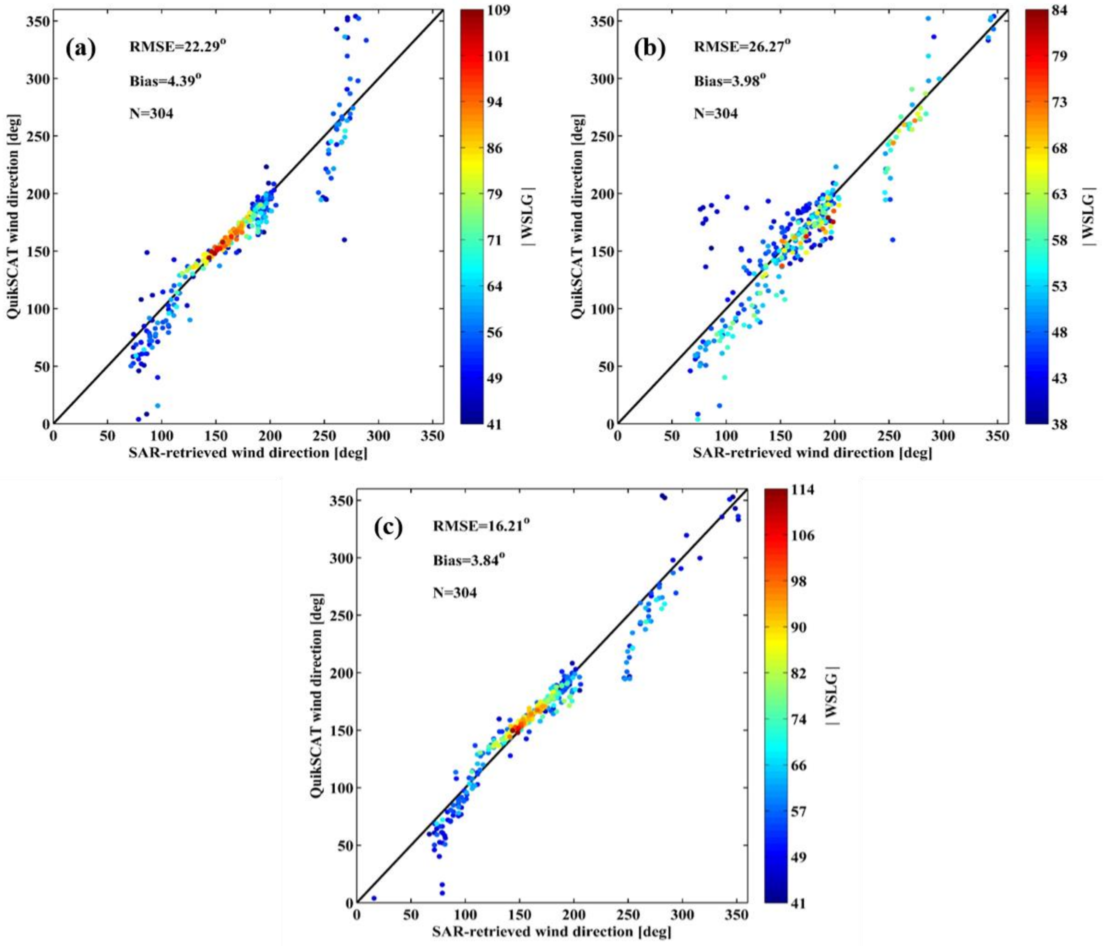

Fig. 12. VV-polarization SAR-retrieved wind directions versus QuikSCAT-measured wind directions, and (b) VH-polarization SAR-retrieved wind directions versus QuikSCAT-measured wind directions, and (c) Dual-polarization (VV+VH) SAR-retrieved wind directions versus QuikSCAT-measured wind directions. Hurricane Bertha wind directions from SAR and QuikSCAT are acquired on July 12, 2008, at 10:14 UTC, and on July 12, 2008, 09:42 UTC, respectively.

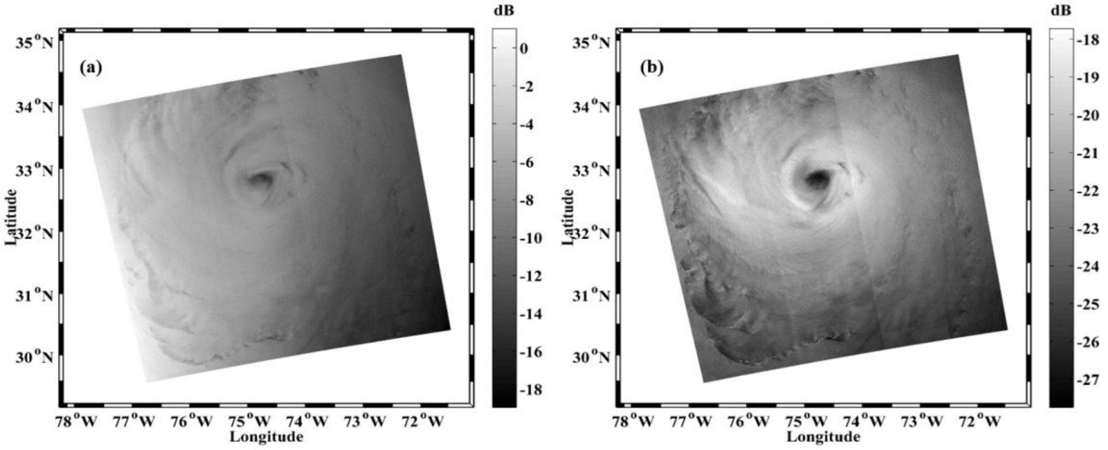

Fig. 13. RADARSAT-2 dual-polarization SAR image acquired over Hurricane Earl on September 2, 2010, at 22:59 UTC showing (a) VV-polarization and (b) VH-polarization, where the color bar shows σ_0 (dB) in VV-polarization (σ_{VV}^0) and in VH-polarization (σ_{VH}^0), respectively. RADARSAT-2 Data and Product MacDonald, Dettwiler, and Associates Ltd., All Rights Reserved.

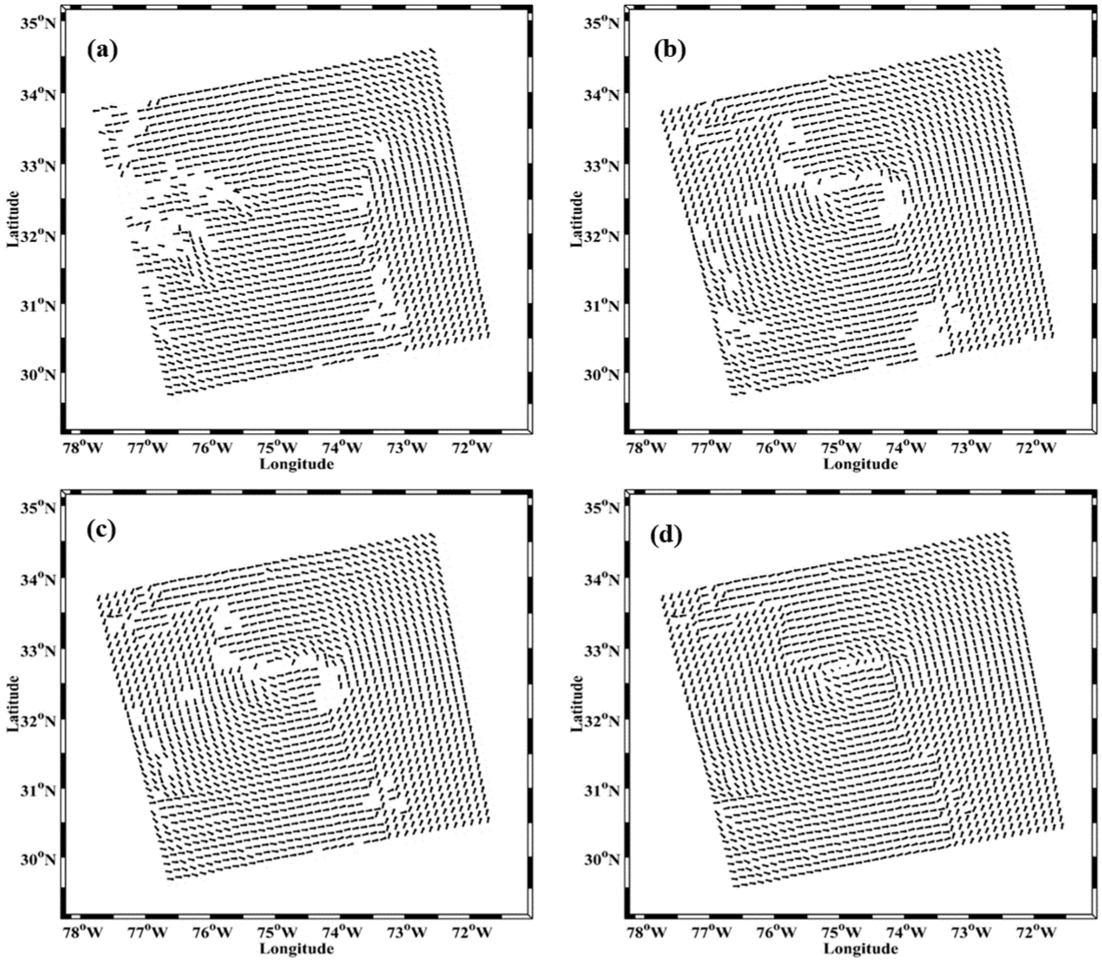

Fig. 14. SAR-retrieved wind directions of Hurricane Earl on September 2, 2010, at 22:59 UTC, with image of (a) VV-polarization, and (b) VH-polarization, and (c) Dual-polarization (VV, VH), and (d) Dual-polarization (VV+VH) and interpolation processing.

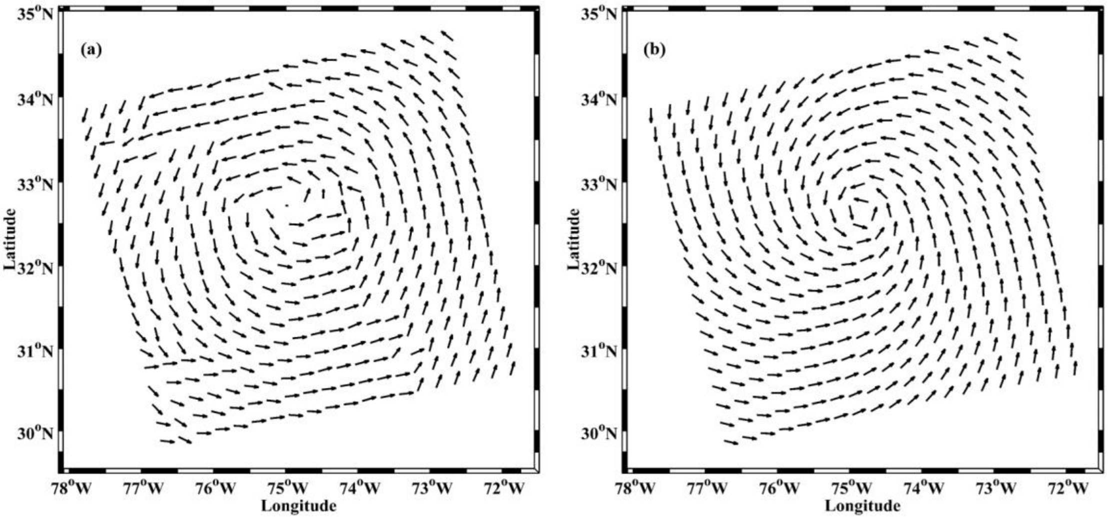

Fig. 15. (a) Dual-polarization SAR-retrieved wind directions of Hurricane Earl on September 2, 2010, at 22:59 UTC. (b) H*Wind wind directions on September 2, 2010, at 22:30 UTC.

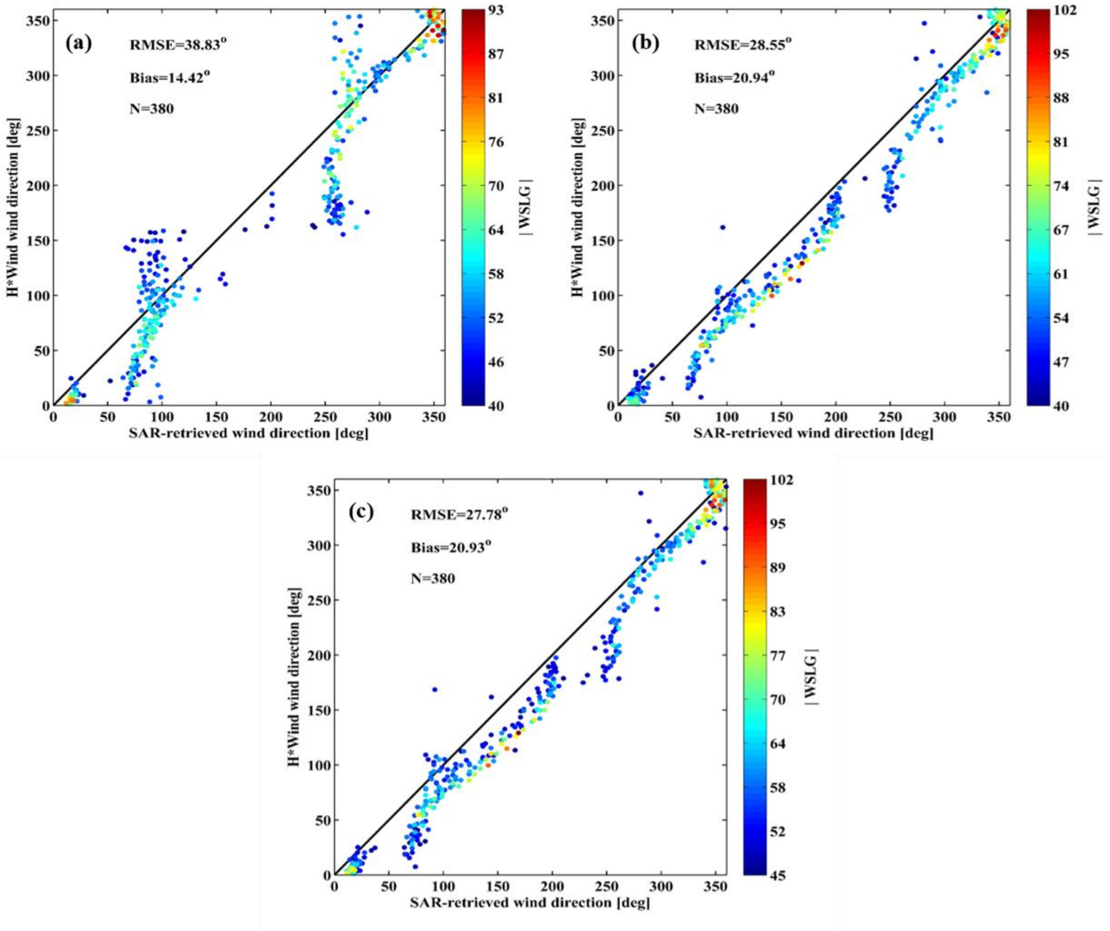

Fig. 16. VV-polarization SAR-retrieved wind directions versus H*Wind wind directions, and (b) VH-polarization SAR-retrieved wind directions versus H*Wind wind directions, and (c) Dual-polarization (VV+VH) SAR-retrieved wind directions versus H*Wind wind directions. Hurricane Earl wind directions from SAR and H*Wind are acquired on September 2, 2010, at 22:59 UTC, and on September 2, 2010, at 22:30 UTC, respectively.

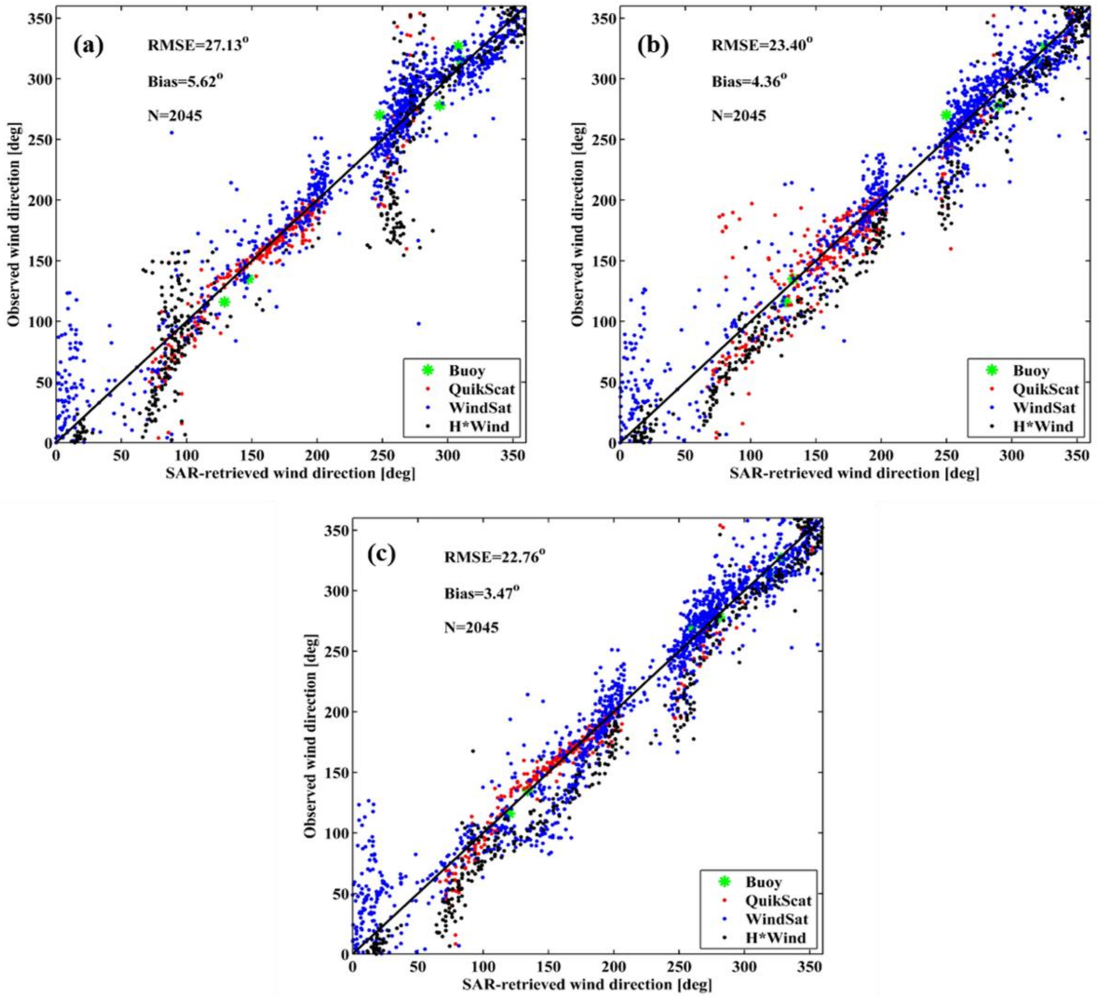

Fig. 17. VV-polarization SAR-retrieved wind directions versus wind directions from buoy, QuikSCAT, WindSat and H*Wind, and (b) VH-polarization SAR-retrieved wind directions versus wind directions from buoy, QuikSCAT, WindSat and H*Wind. (c) Dual-polarization SAR-retrieved wind directions versus wind directions from buoy, QuikSCAT, WindSat and H*Wind.